Adjoint sensitivities of sub-ice shelf melt rates to ocean circulation under Pine Island Ice Shelf, West Antarctica

Patrick Heimbach[1] and Martin Losch[2]

[1] *Massachusetts Institute of Technology, EAPS, Room 54-1518, 77 Massachusetts Avenue, Cambridge, MA 02139, USA*
Phone: +1-617-253-5259; E-mail: heimbach@mit.edu
[2] *Alfred-Wegener-Institut für Polar- und Meeresforschung, Building F-303, Bussestrasse 24, D-27570 Bremerhaven, Germany*
Phone: +49-471-4831-1872; E-mail: Martin.Losch@awi.de

ABSTRACT. We investigate the sensitivity of sub-ice shelf melt rates under Pine Island Ice Shelf, West Antarctica, to changes in the oceanic state using an adjoint ocean model that is capable of representing the flow in sub-ice shelf cavities. The adjoint code is based on algorithmic differentiation (AD) of the Massachusetts Institute of Technology's ocean general circulation model (MITgcm). The adjoint model was extended by adding into the AD process of the corresponding sub-ice shelf cavity code. This code implements a three-equation thermodynamic melt rate parameterization to infer heat and freshwater fluxes at the ice shelf-ocean boundary. The inferred sensitivities reveal a dominant time scale of roughly 60 days over which the shelf exit is connected to the deep interior. They exhibit rich three-dimensional time-evolving patterns that can be understood in terms of a combination of the buoyancy forcing by the inflowing water masses, the cavity geometry, and the effect of rotation and topography in steering the flow in the presence of prominent features in the bedrock bathymetry. Dominant sensitivity pathways are found over a sill as well as "shadow regions" of very low sensitivities. To the extent that these transient patterns are robust they carry important information for decision-making in observation deployment and monitoring.

1. INTRODUCTION

The advent of detailed and continuous satellite observations since the early 1990s has vastly expanded our knowledge of changes occurring in the polar ice sheets. Among the strongest signals observed are changes near their marine margins [Pritchard and others 2009]. In West Antarctica, where fast flowing ice streams feed large ice shelves which are grounded deep below sea level and support vast floating tongues, a region exhibiting one of the largest changes in terms of ice sheet acceleration, thinning, and mass loss is the Pine Island Glacier (PIG) [Hellmer and others 1998, Rignot 1998, Shepherd and others 2001, Joughin and others 2003]. Its extensive ice shelf tongue, the Pine Island Ice Shelf (PIIS), is in direct contact with the ocean in the Amundsen Sea Embayment (ASE). Observed flow speeds are on the order of $3\,\mathrm{km\,a^{-1}}$, under-ice shelf melt rates reach $60\,\mathrm{m\,a^{-1}}$ near the grounding zone and between 20 and $30\,\mathrm{m\,a^{-1}}$ averaged over the ice shelf, associated net thinning amount to 3 to $6\,\mathrm{m\,a^{-1}}$, and mass discharge is between 15 and 35 $\mathrm{Gt\,a^{-1}}$ [Wingham and others 1998, Rignot 2006, Velicogna and Wahr 2006, Rignot and others 2008, Wingham and others 2009]. Attempts to discern potential causes of these observed changes are complicated by the limited period over which satellite data are available (1992 onward for InSAR and radar altimetry from ERS-1/2 and ENVISAT, 2003 onward for gravity field changes from GRACE, 2003 to 2009 for laser altimetry from ICESat). Early glaciological studies combined surface velocity observations with ice flow models to assess the role of basal conditions in setting Pine Island's fast ice stream flow [Vieli and Payne 2003], but the apparent collocation between regions of largest acceleration and their direct contact with the ocean through large ice shelves also suggests a significant contribution of oceanic processes to determining the glacial flow. This link is increasingly being recognized within the glaciological community [Payne and others 2004, Shepherd and others 2004, Thomas and others 2004] and has spurned intense interest in ice sheet-ocean interactions.

Several recent field programs [Jenkins and others 2010a] focused on the PIG and the surrounding ASE to shed light on the detailed circulation, water mass properties, as well as bathymetry and cavity geometry in the Pine Island embayment. These campaigns have been motivated by modelling efforts that tried to quantify ocean-induced melt rates under the PIIS in the context of recent changes in water mass properties in the ASE [Payne and others 2007].

Modelling ocean-induced melt rates go back to at least the 1970s, when Robin [1979] conjectured that the shape of sub-ice shelf cavities might be strongly influenced by heat and freshwater delivery to its base, and the detailed patterns of subsequent sub-ice shelf melting and refreezing effects. The initially simple parameterizations of melt rates have evolved over time into what is now referred to as a three-equation thermodynamic model [Hellmer and Olbers 1989, Jenkins and Bombosch 1995, Holland and Jenkins 1999]. This model solves two conservation equations for heat and freshwater flux at the ice-ocean interface under the constraint that the ice boundary is at the pressure melting point (third equation). The total heat flux takes into account the ice-ocean temperature difference, a contribution from latent heat of fusion and heat diffusion through the ice shelf. The transfer coefficients (or implied piston velocities) employed in these parameterizations are either assumed constant or parameterized in terms of a boundary layer friction velocity [Holland and Jenkins 1999] adopted from sea-ice modelling

[McPhee and others 1987]. Direct observations, however, of melt rates are rare because of the technological challenge to obtain them. This places large uncertainties on all current approaches [Holland and others 2008], and thus on magnitudes of melt rates.

Recognizing melt rate uncertainties as a serious gap in the chain which may link observed oceanic changes and ice shelf thinning raises the question to which extent ocean hydrographic observations away from the ice-ocean boundary, which may be easier to obtain, are useful to constrain melt rates. The present study is a first step toward addressing this problem from an inverse modelling perspective. Using an ocean general circulation model with realistic topography of the Pine Island embayment and geometry of the PIIS, we present comprehensive sensitivity patterns of sub-ice shelf melt rates to changes in ocean circulation. The sensitivities are obtained with an adjoint model of a full-fledged ocean GCM that resolves the sub-ice shelf circulation and includes a thermodymamic melt rate parameterization [Losch 2008]. The sensitivities serve several purposes:

(1) they identify dominant water mass pathways, time scales, and dynamical processes which affect melt rates;

(2) they carry information which may be useful for guiding oceanographic field campaigns which seek to deploy limited measurement assets in an optimal manner;

(3) as a foundation for subsequent studies, they establish the feasibility of connecting hydrographic observations to constrain melt rates in formal estimation approaches such as undertaken within the ECCO consortium [Wunsch and Heimbach 2007, Wunsch and others 2009].

We realize that inferred melt rate sensitivities are dependent upon the parameterizations used, but regard this as an asset down the road when sensitivities are used for inverse calculations in which a model vs. data misfit reduction is sought. Unrealistic melt rate parameterizations may lead to unrealistic sensitivity fields whose use in a gradient-based optimization would fail to achieve the desired misfit reduction.

The remainder of the paper is organized as follows: We first provide a description of the model, its adjoint, and its configuration in the Pine Island embayment (Section 2). Results from adjoint-based sensitivity calculations are presented in Section 3. A discussion is given in Section 4 along with some conclusions in view of the prospect of adjoint-based melt rate estimation.

2. MODEL DESCRIPTION

2.1. Forward model

The Massachussetts Institute of Technology general circulation model [MITgcm, Marshall and others 1997a,b] is a state-of-the-art scalable finite-volume numerical ocean general circulation model. In the configuration of this study, the model solves the Boussinesq, hydrostatic so-called primitive equations of ocean dynamics on a horizontal curvilinear grid on the rotating sphere and on vertical geopotential height surfaces ("z"-levels) in a regional domain with open boundaries. General information about the code can be found at `http://mitgcm.org` [MITgcm Group 2011].

The model is the first z-coordinate model with the capability to simulate the circulation in sub-ice shelf cavities [Losch 2008]. The sub-ice shelf package consists of two main parts:

(1) MITgcm's partial cell implementation to more accurately represent topography [Adcroft and others 1997] was extended to represent circulation in a cavity;

(2) a tree-equation melt rate parameterization to simulate melting at the ocean-ice interface and associated freshwater fluxes into the ocean [Hellmer and Olbers 1989, Jenkins and others 2001].

Details of this parameterization are summarized in the Appendix.

2.2. Adjoint model generation

The use of adjoint models for estimation or data assimilation has a long tradition in meteorology (e.g., Le Dimet and Talagrand [1986], Talagrand and Courtier [1987]), oceanography (e.g., Tziperman and Thacker [1989], Marotzke and Wunsch [1993]), and glaciology (e.g., MacAyeal [1992, 1993]). We limit ourselves here to an abbreviated introduction.

2.2.1. Why adjoints?

The present study is focussed on how sub-ice shelf melt rates change as a result of changes in the local and remote ocean circulation. Formally, obtaining a comprehensive set (or field) of sensitivity information amounts to computing the gradient of an objective function with respect to a very high-dimensional control space spanning the full time-varying three-dimensional oceanic state. For the case of PIIS, the objective function J is chosen as the total melt rate integrated over the entire sub-ice shelf-ocean boundary $\int \mathrm{dA}$, and averaged over a period $\Delta\tau$ preceding the final time τ_f:

$$J = \frac{1}{\Delta T} \int_{\tau_f - \Delta\tau}^{\tau_f} \int_{dA} q(\mathbf{x}(t)) \, \mathrm{dA} \, \mathrm{dt} \tag{1}$$

The integrals reduce in practice to a sum over discrete space and time. The local melt rate at each grid point (i, j, k) is the freshwater flux $q(t)$ (expressed here as a volume flux; space indices are dropped). $q(t)$ is a function of the model state $\mathbf{x}(t) = \{T, S, \mathbf{U}, \eta\}(t)$ consisting of all prognostic ocean state variables at time t, i.e. temperature, salinity, three-dimensional velocity, and sea surface elevation. $q(t)$ is obtained from a three-equation melt rate parameterization, eqn. (A1) described in more detail in the Appendix.

In order to simplify the following discussion, we drop the time-average, i.e. consider q at the final time step τ_f of the integration, and assume that we wish to infer the sensitivities of $J(q(\tau_f))$ to changes in the initial condition of the oceanic state $\mathbf{x}(0)$. What we are faced with is the computation of perturbations of the objective function δJ to changes in any element of the control space $x_i(0)$ (the control space is easily extended to allow surface forcing fields, boundary conditions, or model parameters, either spatially constant or varying). The ocean model operator $\mathcal{L}$ carries $\mathbf{x}(0)$ forward from time $t = 0$ to time t through the sequence

$$\mathbf{x}(t) \;=\; \mathcal{L}_t(\mathcal{L}_{t-1}(\ldots(\mathcal{L}_1(\mathbf{x}(0))))).$$

A direct approach to compute the gradient consists of calculating directional derivatives, i.e. perturbing each element $x_i(0)$ of the initial state vector $\mathbf{x}(0)$ (which determine the control space dimension n) separately. A perturbation of an individual melt rate area element $\delta q_i(t)$ obtained from perturbing the initial state element $x_i(0)$ has the form

$$\begin{aligned}
\delta q_i(t) &= \frac{\partial q(t)}{\partial \mathbf{x}(t)} \cdot \frac{\partial \mathbf{x}(t)}{\partial \mathbf{x}(t-1)} \cdot \ldots \cdot \frac{\partial \mathbf{x}(1)}{\partial x_i(0)} \delta x_i(0) \\
&= \frac{\partial q(t)}{\partial \mathbf{x}(t)} \cdot L \cdot \delta x_i(0) \\
&= \frac{\partial q(t)}{\partial \mathbf{x}(0)} \cdot \delta x_i(0)
\end{aligned} \tag{2}$$

for unit perturbations $\delta x_i(0)$. Here,

$$\begin{aligned}
L \;=\; L_t \cdot \ldots \cdot L_1 &= \frac{\partial \mathbf{x}(t)}{\partial \mathbf{x}(t-1)} \cdot \ldots \cdot \frac{\partial \mathbf{x}(1)}{\partial \mathbf{x}(0)} \\
&= \frac{\partial \mathcal{L}_t}{\partial \mathbf{x}(t-1)} \cdot \ldots \cdot \frac{\partial \mathcal{L}_1}{\partial \mathbf{x}(0)}
\end{aligned} \tag{3}$$

is the tangent linear model (or model Jacobian) of the full ocean GCM operator $\mathcal{L}$. The full n-dimensional gradient can then be assembled from all separately calculated elements δq_i. For large scale problems, where each forward calculation on its own is CPU intensive, and where the control space dimension is large (the dimension of the initial temperature field of the $(1/32)^\circ$ configuration described in section 2.3 is $N_x \times N_y \times N_z = 100 \times 120 \times 50 = 6 \times 10^5$), this direct approach for obtaining the full gradient is not tractable. This is true, regardless of whether the exact tangent linear operator of J is used, or whether it is computed through finite-difference approximations of the form $\frac{J(x+\epsilon)-J(x)}{\epsilon}$.

Re-casting eqn. (2) as a scalar product and using the formal definition of the adjoint operator $< x, Ly >=< L^T x, y >$,

$$\begin{aligned}
\delta q(t) &= < \tfrac{\partial q(t)}{\partial \mathbf{x}(t)}^T \;, \; \delta \mathbf{x}(t) > \\
&= < \tfrac{\partial q(t)}{\partial \mathbf{x}(t)}^T \;, \; L \cdot \delta \mathbf{x}(0) > \\
&= < L^T \cdot \tfrac{\partial q(t)}{\partial \mathbf{x}(t)}^T \;, \; \delta \mathbf{x}(0) > \\
&= < \tfrac{\partial q(t)}{\partial \mathbf{x}(0)}^T \;, \; \delta \mathbf{x}(0) >
\end{aligned} \tag{4}$$

where for a finite dimensional real vector space the adjoint operation reduces to the transpose L^T, makes it possible to compute the gradient in one single simulation:

$$\begin{aligned}
\frac{\partial q(t)}{\partial \mathbf{x}(0)}^T &= L^T \cdot \frac{\partial q(t)}{\partial \mathbf{x}(t)}^T \\
&= \frac{\partial \mathbf{x}(1)}{\partial \mathbf{x}(0)}^T \cdot \ldots \cdot \frac{\partial \mathbf{x}(t)}{\partial \mathbf{x}(t-1)}^T \cdot \frac{\partial q(t)}{\partial \mathbf{x}(t)}^T
\end{aligned} \tag{5}$$

Important points to note are:

(1) In the same way that the tangent linear model (TLM) L carries small perturbations $\mathbf{x}(0)$ of the initial state *forward* to perturbations in $q(t)$, the adjoint model (ADM) carries sensitivities of $q(t)$ to $\mathbf{x}(t)$ *backward* to sensitivities of $q(t)$ to the initial state $\mathbf{x}(0)$. Put differently, the TLM yields the impact of changes in *one input* on all outputs, whereas the ADM is used to infer how one output is influenced by *all inputs*.

(2) Since the tangent linear and adjoint operators L, L^T of the MITgcm are already available, eqn. (2) and (5) indicates that the work of obtaining a sub-ice shelf cavity enabled GCM is incremental, consisting mainly of the generation of an adjoint for the operators $\partial q(t)/\partial \mathbf{x}(t)$, which connect the model derivative at any time t to the melt rate derivative.

(3) Eqn. (5) implies that the adjoint integration occurs in reverse, carrying the sensitivities $(\partial q(t)/\partial \mathbf{x}(t))^T$ at time $t = \tau_f$ to time $t = 0$. It also implies that intermediate sensitivities at any time t are calculated and can be saved (e.g., for transient sensitivity analyses) within the integration.

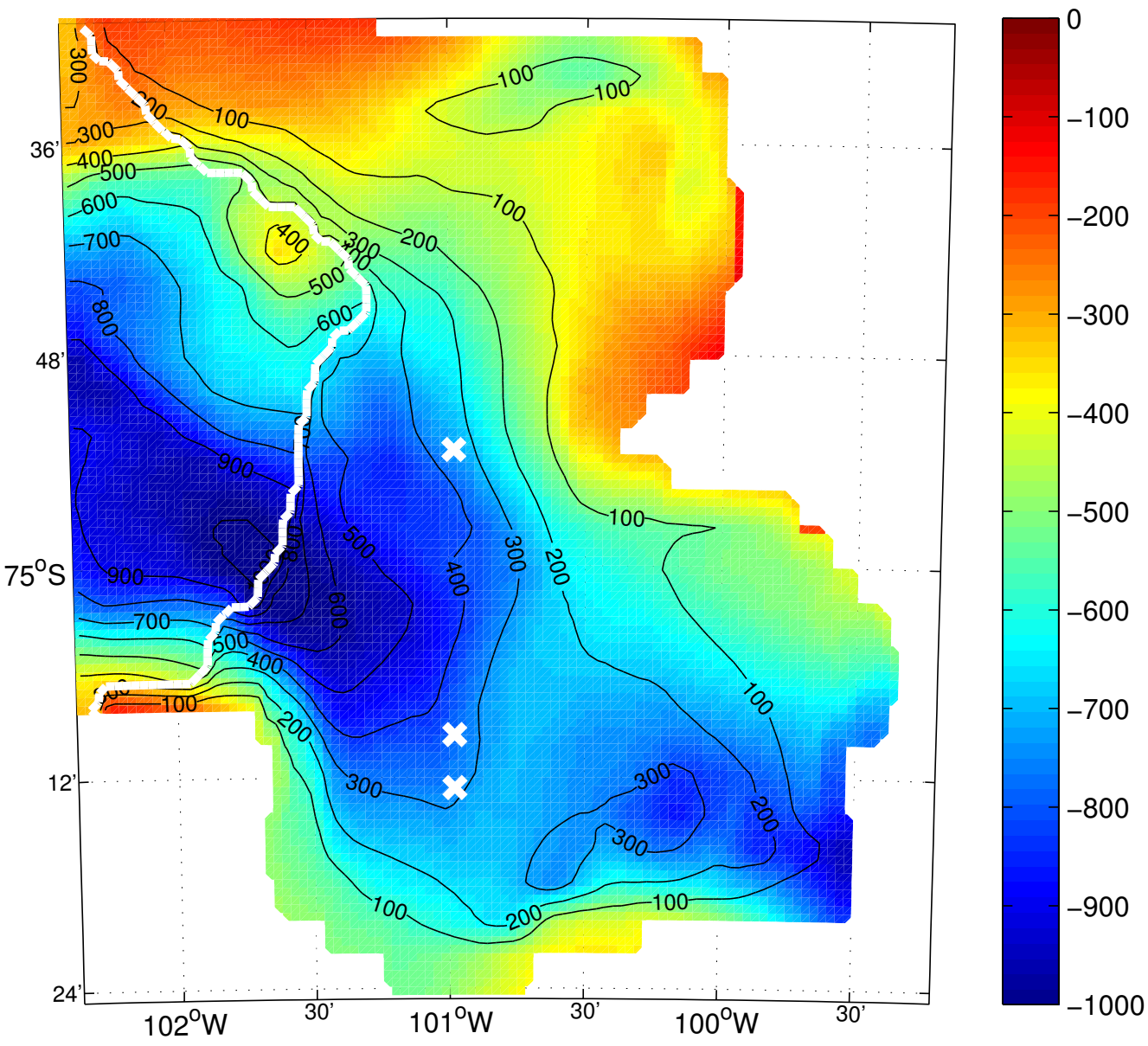

Fig. 1. Bed rock bathymetry (color, in meters) and water column thickness (contours, in intervals of 100 m) of the (1/32)° (900±30 m) horizontal resolution model. The white contour indicates the ice edge, the white X-es the position of the three hypothetical drilling sites in Section 3.3.

2.2.2. Use of algorithmic differentiation (AD)

Rigorous application of algorithmic or automatic differentiation (AD) [Griewank and Walther 2008] is key to the adjoint code generation of the MITgcm. The model has been developed from the outset with the perspective that adjoint modelling would be a key application [Marotzke and others 1999]. The AD tool used initially was the "Tangent linear and Adjoint Model Compiler" (TAMC) of Giering and Kaminski [1998]. Care was taken that coding was compatible with the AD tool's language parsing and active flow dependency analysis capabilities and limitations. The two major initial applications were the use of the MITgcm adjoint to investigate Atlantic meridional heat transport sensitivities [Marotzke and others 1999], and the use of the gradient of a least-squares model vs. data misfit cost function in a gradient-based optimization of the MITgcm to available satellite and in-situ observations as part of the "Estimating the Circulation and Climate of the Ocean" (ECCO) consortium [Stammer and others 2002a,b].

Over the last decade, in a strongly symbiotic effort, both the MITgcm as well as the AD tool have evolved and matured significantly. The MITgcm evolved from a code optimized for vector machines to a code that can be adapted to various vector and parallel high performance computing architectures by means of a flexible domain decomposition. The support routines in which the adjoint inherits the same domain decomposition of the forward model [Heimbach and others 2005] is the only part of the MITgcm that is hand-written. The MITgcm has arguably pushed the limits of the AD tool, which in turn has matured as a result, and is now known in its commercial version as "Transformation of Algorithms in Fortran" (TAF) [Giering and others 2005].

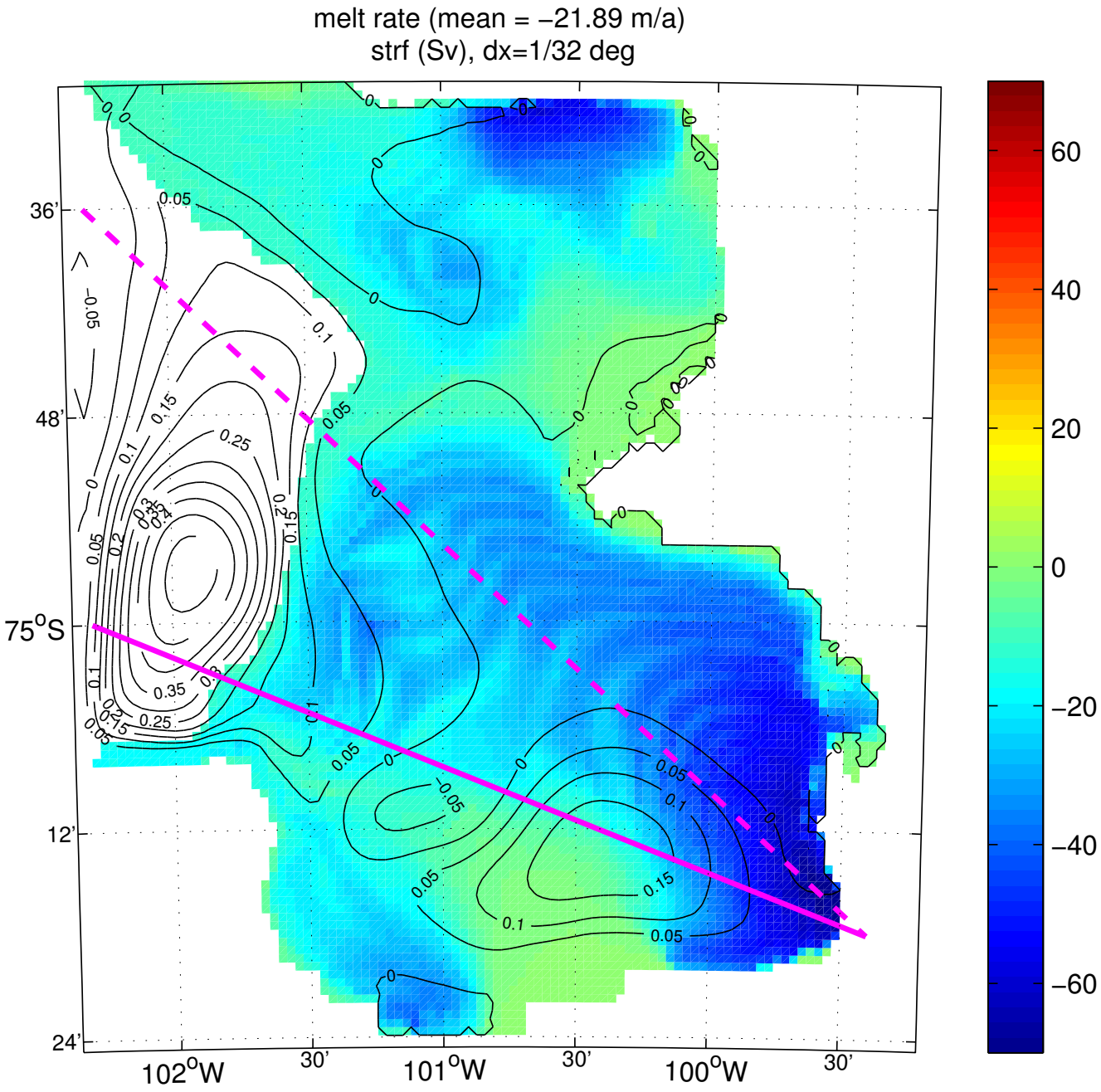

Fig. 2. Mean melt rate (in color, in $\mathrm{m\,a^{-1}}$) and vertically integrated stream function (contours, in intervals of 0.05 Sv, 1 Sv = 10^6 $\mathrm{m^3/s}$). The cyan lines show the location of Section 1 (solid) and Section 2 (dashed).

The AD approach has ensured that over time the adjoint model has kept up-to-date with various forward model improvements, the inclusion of new model packages, and application of the adjoint to various problems (for a recent overview of examples see Heimbach [2008]). Various tutorial introductions to AD in the context of ocean and ice sheet modelling are today available (e.g., Giering and Kaminski [1998], Marotzke and others [1999], Wunsch [2006a], Heimbach and Bugnion [2009]), and the MITgcm online manual has a dedicated chapter on this subject (see chapter 5 of MITgcm Group [2011]). It is crucial to realize that there is no unique adjoint model. Its structure and detail will depend on the application, in particular on the choice of objective function and control variable, as described, e.g. in Losch and Heimbach [2007].

In the context of AD of the sub-ice shelf cavity capability, the general structure of the MITgcm is important. Because the sub-ice shelf cavity capability is implemented as a separate package, the adjoint development largely consisted in the *incremental* work to ensure that the package is properly handled by the AD tool and that correct and *efficient* adjoint code is generated.

2.3. Pine Island Ice Shelf configurations

The domain chosen for our simulation is the immediate surrounding of the Pine Island Ice Shelf (PIIS) in the Amundsen Sea Embayment, covering an area of 90×108 $\mathrm{km^2}$, between roughly 74°3'S and 75°2'S, and 102°2'W and 99°1'W in latitudinal

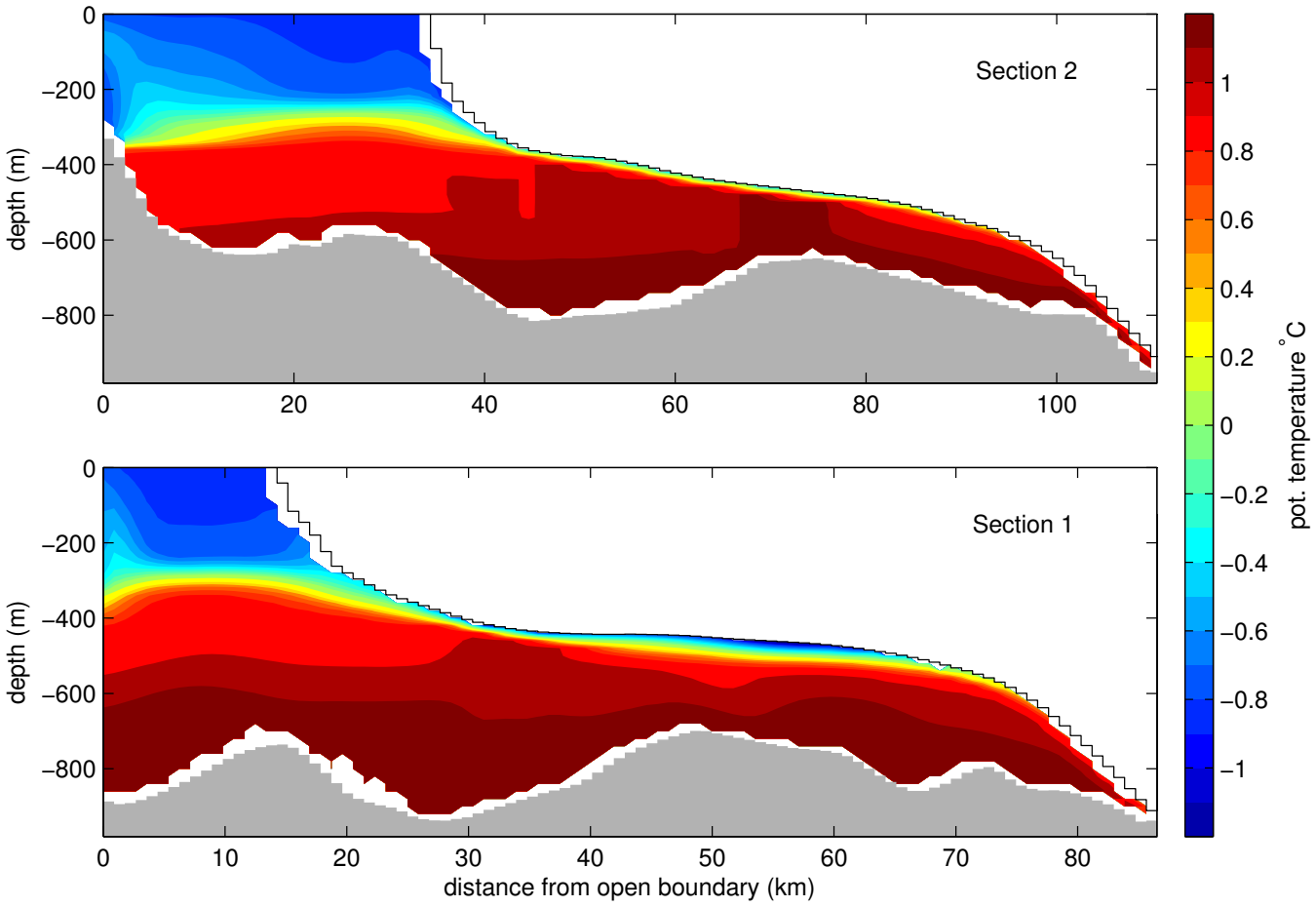

Fig. 3. Potential temperature distribution (color, in °C) along Section 1 and 2, as shown in Fig. 2.

and longitudinal extent. The domain covers the entire floating ice shelf. It has one open boundary to the West with the wider Amundsen Sea Embayment.

We present a high-resolution configuration at $(1/32)^\circ$ corresponding to 900±30 m cell widths. Coarse-resolution configurations are also available as they remain practical for global coupled climate simulations for the time being, but are not shown here. The configuration has an evenly-spaced vertical grid consisting of 50 vertical z levels of 20 m cell thicknesses. The high vertical resolution ensures that the temperature gradient under the ice shelf is well represented. More numerical details are summarized in Table 1.

The high-resolution adjoint setup was configured to run in parallel on 16 processors, with the full domain ($Nx \times Ny = 100\times120$) decomposed into 16 tiles of size $Nx \times Ny = 25\times30$ each (the choice of tile size represent a tradeoff between on-processor FLOPS versus cross-processor communication requirements per time step). Note that the use of AD ensures that the adjoint model inherits the same domain decomposition scalability of the forward model.

Bathymetry and cavity geometry as obtained from Timmermann and others [2010] are shown in Fig. 1. All adjoint calculations start from a 10-year spin up. The spin up itself was initiated from climatological fields for temperature and salinity based on recent auto-sub measurement [Jenkins and others 2010a] with open boundary conditions that are estimated from in-situ data (5 hydrographic stations along the edge of the ice shelf, Mike Schröder, AWI, personal communication). The adjoint calculations were performed over a one-year period. The integrations consist of a forward integration to establish the model state around which the model is linearized, i.e. for which all adjoint derivative expressions are evaluated. Snapshots of the adjoint state (i.e. the sensitivities) are saved at two-day intervals to enable detailed transient sensitivity analyses.

3. RESULTS

3.1. Forward solution

Fig. 2 shows the mean melt rate (in color) and vertically integrated stream function (contours, with interval of 0.05 Sv, 1 Sv = 10^6 m^3/s). Time averaged potential temperature distribution (in °C) along the dashed (top) and solid (bottom) lines (Sections 1 and 2) defined in Fig. 2 are depicted in Fig. 3. The time and space averaged fresh water flux (melt rate) is roughly -22 m a^{-1} (fresh water flux is positive upward so that negative values correspond to ocean freshening). The layering of deeper (below roughly 400 m) warm water (attributed as Circumpolar Deep Water) underneath colder surface waters is clearly visible in Fig. 3. Maximum melt rates are found in the southeastern as well as northeastern corners. In these regions the ice-ocean

interface reaches below roughly 500 m depth (cf. Fig. 1), and ocean temperatures at the interface exceed roughly 0.5°C. There is a cyclonic gyre in the open ocean that barely enters the cavity and a second one in the southeastern cavity. These gyres are connected by a third anti-cyclonic gyre over the bottom topography ridge in the bed-rock bathymetry at 101°W that is described in Jenkins and others [2010a].

3.2. Adjoint sensitivities

For each variable of the forward model state there exists a dual variable of the adjoint model state. Focussing most of our discussion on temperature $T(i,j,k,t)$ at each point in space (i,j,k) and time t, the corresponding adjoint variable $\delta^* T(i,j,k,t)$ is the gradient of objective function J with respect to T at position (i,j,k) and time t:

$$\delta^* T(i,j,k,t) = \frac{\partial J}{\partial T}^T \Big|_{i,j,k,t}.$$

We wish to provide some insights, both into the spatial structure of these gradients and their transient behavior. To do so, we show in Fig. 4 adjoint sensitivities $\delta^* T(i,j,k,t)$ for different time snapshots as horizontal slices at two depth levels (left two columns), and as vertical sections along the two diagonal Sections indicated in Fig. 2 (right two columns). For clarity, the section lines are also drawn in the horizontal slices, and the two depth levels are marked in the vertical sections. Noting again the reverse nature of the adjoint integration (eqn. 5) and the period over which we evaluate the objective function to be the last 30 days of the integration (eqn. 1), i.e. from $\tau_f - 30$d to τ_f, we show, from top to bottom, sensitivities 10, 30, and 60 days back in time from τ_f. Overall, sensitivities are predominantly negative, indicating an increase in melt rates with increasing temperatures (negative values of q correspond to freshening of the ocean).

As a note on terminology, the interpretation of adjoint sensitivities which are integrated *backward* in time is frequently mixed with their translation into the evolution of perturbations *forward* in time. Thus, in analyzing transient behavior and time evolution we usually imply *backward-in-time evolution* when describing *sensitivity* propagation (top to bottom in the figures), but *forward-in-time evolution* when discussing the propagation of *perturbations*.

As a context for interpretation, we recall that melt rates are largest in the southeastern and northeastern corners of the domain (cf. Fig. 2). Therefore the sensitivities at the beginning of the backward integration are confined mostly to these areas, and spread out over backwards-running time. Our discussion focusses on two broad sensitivity patterns, one emerging from the northern mid-depth part, and one from the southeastern deep interior of the cavity. We gain insight into the dominant pathways by following the sensitivities backward in time.

By $\tau_f - 10$ days the southeastern sensitivity pattern has started to move (backwards) with the interior-cavity cyclonic gyre and then the anti-cyclonic gyre across the ridge at 101°W. At this time the sensitivities are mostly found near the ice-ocean interface, as the objective function J is an average over the last 30 days of the integration. The northern sensitivity pattern evolves more slowly because the forward circulation is weaker.

By $\tau_f - 30$ days the southeastern sensitivity below 400 m has moved further towards the western open boundary of the domain, while some of the northern sensitivity has already reached the boundary in a narrow strip around 300 m depth. Because the objective function J is a time mean over this time interval, the sensitivities are accumulated over this period, and which explains the persistent (apparently stationary) sensitivity deep inside the cavity.

By $\tau_f - 60$ days the sensitivity amplitudes in the cavity's deep interior have subsided because the objective function stopped "measuring" melt rates at $\tau_f - 30$ days. This means that no local perturbations inside the cavity can influence melt rate significantly, and that remote perturbations dominate changes in melt rates on this time scale. Some of the melt rate sensitivities, especially at shallower depths have moved across the open boundary out of the domain. Note that there are regions in the model domain through which the high-amplitude sensitivity patterns never pass.

The large differences in patterns along the two vertical sections illustrate the high spatial variability of the sensitivity pathways. The adjoint sensitivities follow the reverse flow that is topographically steered by the sill at roughly 700 m depth. Instead of propagating along the northern cavity boundary, the sensitivities in the horizontal map turn at the sill. This turn is the same deflection, albeit in reverse direction, that flow in rotating frames of reference undergoes in order to preserve potential vorticity (compensation of vortex stretching through changing relative vorticity of the water column) when it encounters changing topography. Indeed, the sensitivity tells us that a perturbation applied to the forward model to the west of the sill near the southern boundary would be deflected northward after crossing the sill, and a perturbation entering the deep cavity interior near its northern boundary would be deflected southward on reaching the sill and then northwards after crossing it.

Sensitivities with respect to salinity ($\delta^* S = (\partial J/\partial S)^T$) have a very similar pattern as temperature but with reversed sign (not shown), so that lower salinity and higher temperature at a given point imply larger melt rates. Physically, lower salinity and higher temperature imply more buoyancy. Less buoyant (more saline) water cannot rise as far along the inclined ice-ocean interface and thereby reduces the contact time of warm water with ice. In contrast, more saline water also reduces the freezing point of sea water leading to more melting. The sign of the adjoint sensitivities with respect to salinity indicates that the buoyancy effect due to salinity dominates over the freezing point effect. This is explored in more detail in the appendix.

3.3. Perturbation experiments and implications for monitoring

The rich information contained in the sensitivity maps can be explored in a variety of ways. Here we sketch how one could take advantage of adjoint sensitivity information in the planning of an observational campaign.

Consider an expedition to the Pine Island Ice Shelf with the goal of measuring near and under-ice shelf hydrography via CTD casts, drilling through the ice shelf, and Autonomous Underwater Vehicle (AUV) deployment. In choosing the drilling location, a variety of criteria have to be considered and balanced. Among them is the choice of a position that is well-suited

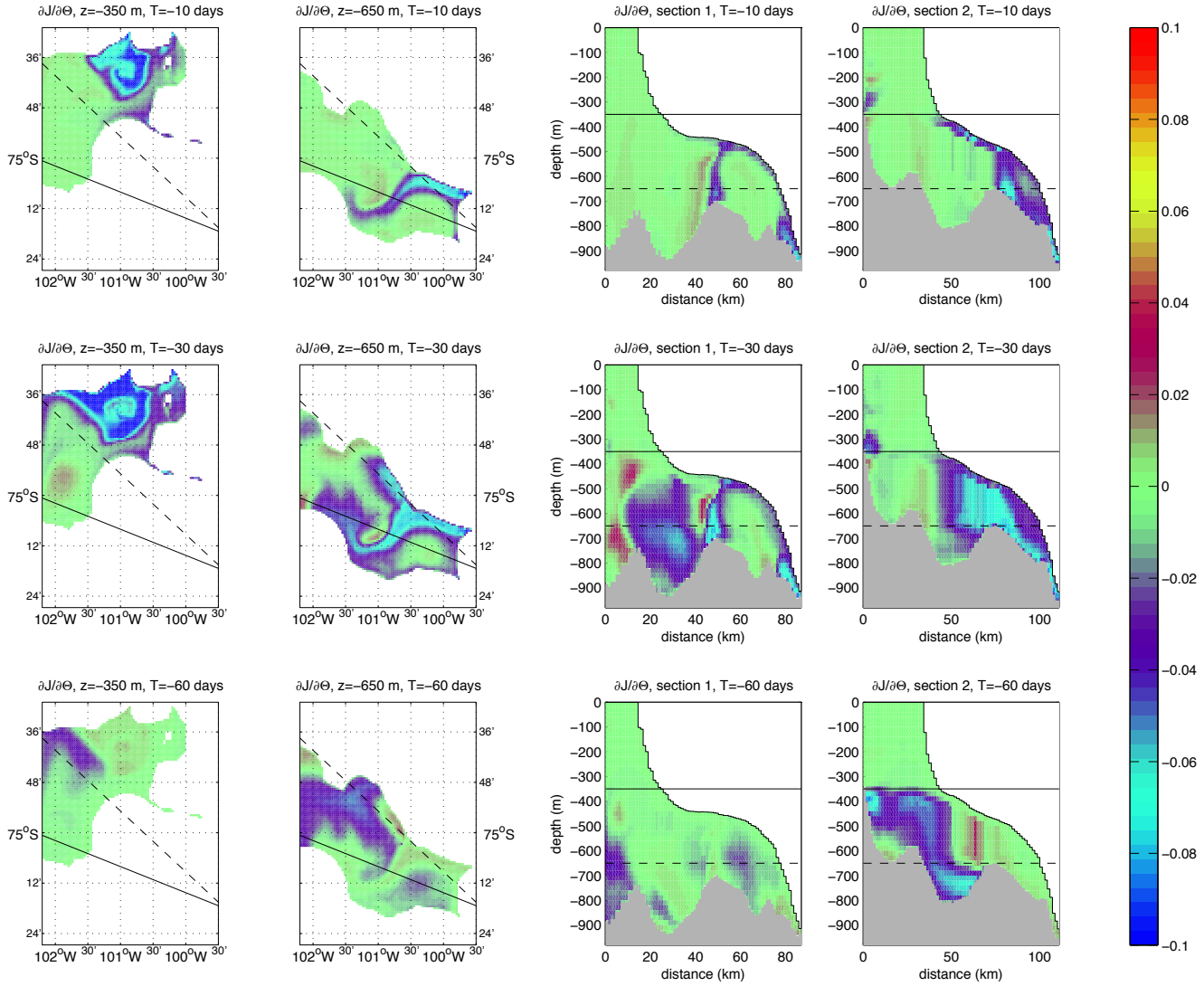

Fig. 4. Adjoint sensitivities $\delta^* T = (\partial J \partial T)^T$ at $t = \tau_f - 10$ days, -30 days, and -60 days. Horizontal slices at $z = -350$ m and $z = -650$ m on the left hand side, vertical sections on the right hand side. The solid lines in the horizontal slice plots indicate section 1 (right-center), and the dashed lines section 2 (far right). The solid and dashed lines in the vertical section plots indicate the positions of the horizontal slices. Units are in $\mathrm{m^3\,s^{-1}\,K^{-1}}$, 0.1 $\mathrm{m^3\,s^{-1}\,K^{-1}} \approx 3\ \mathrm{Mt\,a^{-1}\,K^{-1}} \approx 3\ \mathrm{mm\,a^{-1}\,K^{-1}}$.

for connecting (i.e. correlating) local hydrographic measurements to melt rates. How can the adjoint melt rate sensitivities support the choice of suitable positions?

To address this question, we have plotted in Fig. 5 three vertical profiles of melt rate sensitivities as a function of time, whose choice was guided by the sensitivity maps, Fig. 4. The profiles' positions along 101°W, a meridian crossing the prominent sill in the cavity, are marked in Fig. 1 as white "X"-es. In Fig. 4, at τ_f - 30 d and between 600 and 650 m depth, a southern position at 75.21°S indicates a strong negative sensitivity (southern tip of the "loop" located across the sill), whereas a position slightly further to the north (75.16°S) suggests a slightly positive sensitivity (i.e. an increase in temperature there would *decrease* the melt rate). Proceeding further north, the sign reverts yet again, such at at 74.89°S a moderate negative sensitivity is again visible. The corresponding time series of the three profiles in Fig. 5 illustrate the sensitivity evolution and its vertical structure.

The behavior, especially of the sign reversal along the 101°W meridian, may be surprising and warrants independent testing to confirm the adjoint results. To do so, we conducted a separate forward finite-difference perturbation experiment for each of the three locations. The calculation consisted of re-starting the *forward* model from time $\tau_f - 26$ days, but applying a temperature perturbation of $\Delta T = +0.3$°C in a three-dimensional box of 4×4×4 grid points centered around each individual location (identical longitudes, 101°W, and depth levels 640 m). The resulting melt rate anomalies with respect to the unperturbed ones are plotted in Fig. 6 as a function of time over the final 26-day time interval. These experiments, which do not use the adjoint model, confirm the "predictions" of the adjoint sensitivities, i.e. a strong negative anomaly (significantly increased melt rates) for the southern-most location, a positive anomaly (decreased melt rates) slightly further north, and a moderate (and time-lagged) negative anomaly at the northern-most position. Signs and amplitudes of the adjoint sensitivities at all three locations are thus confirmed via the finite-differences.

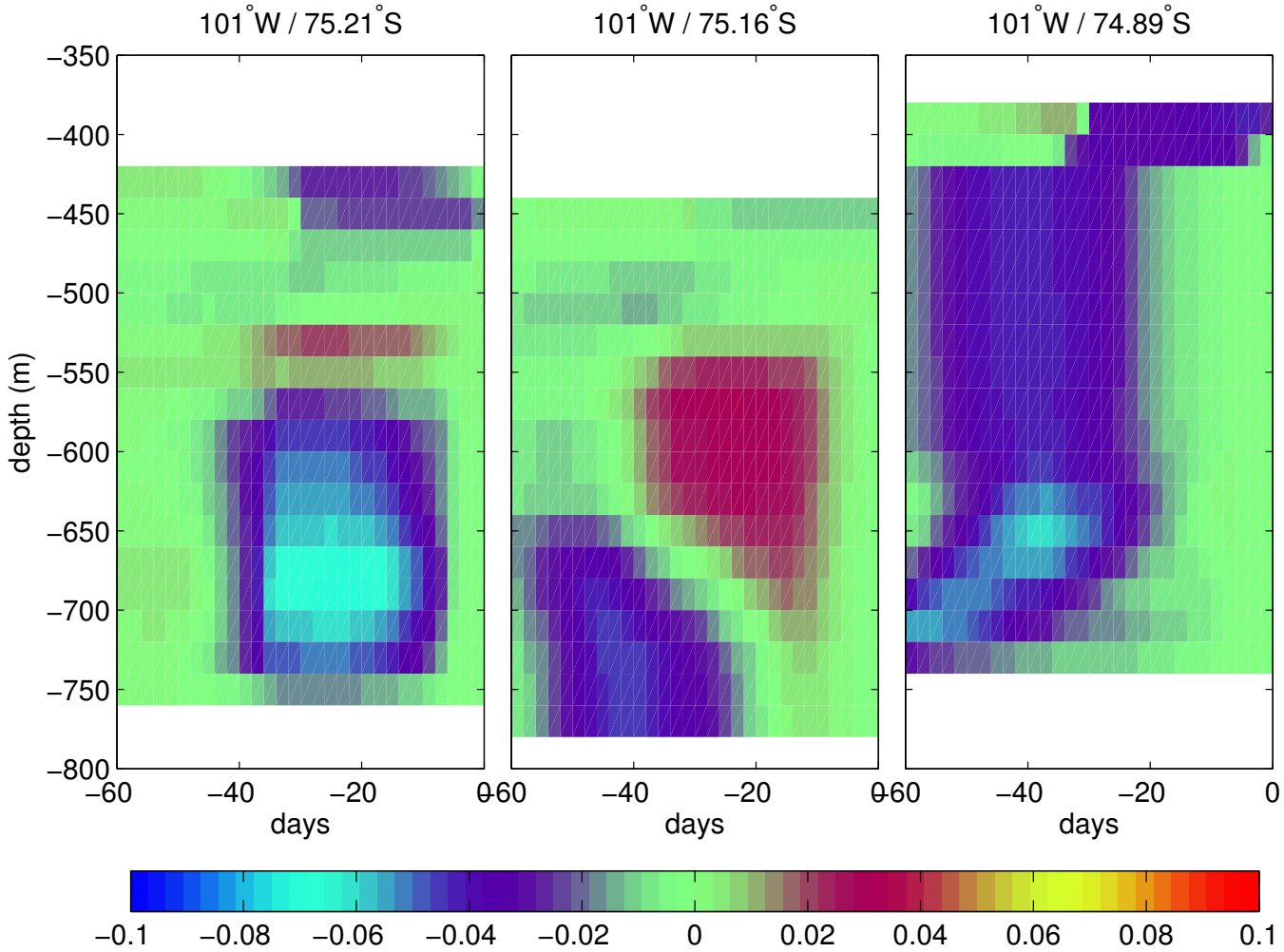

Fig. 5. Vertical sensitivity profiles as a function of time for three locations along the same meridian (101°W). Time is confined to the first 60 days of the adjoint integration. Units are, as in Fig. 4, $m^3\,s^{-1}\,K^{-1}$.

There are significant implications for hydrographic instrument positioning. The strong sensitivity at the southern-most location seems to make it an efficient location if melt rate variability is to be inferred from or correlated with these measurements. In contrast, measurements of a 0.3°C temperature increase obtained slightly further to the north would be highly misleading if interpreted naively as connecting increased temperatures to increased melt rates.

There are caveats. The sensitivities are model-based, and corroboration is needed of

(1) whether the model represents the regional circulation with sufficient skill, and

(2) how robust the sensitivity patterns are in the face of realistic hydrographic variability.

Preceding the sensitivity calculation by an estimation study is an attractive strategy for (1). Such an estimate makes available a reference state that has been fit to the already available observations. Dealing with (2) could entail an ensemble of sensitivity studies for perturbed baseline trajectories to assess which patterns are robust (e.g., determined more by local topography than hydrographic variability), or recurring (e.g., predominant circulation). In any case, conducting a comparatively cheap modelling study as presented here seems warranted in the mix of decision tools for planning a comparatively expensive expedition such as the one imagined.

4. DISCUSSION AND CONCLUSION

Following the first implementation of sub-ice shelf cavity circulation and melt rate parameterization in a z-coordinate model [Losch 2008], we have extended the MITgcm's adjoint capability by including the corresponding code package in the adjoint code generation procedure. Rigorous application of algorithmic differentiation (AD) made the required development straightforward, and only incremental steps were required in adjusting the code package.

The adjoint's utility was demonstrated through studying melt rate sensitivities under Pine Island Ice Shelf, West Antarctica, to changes in sub-ice shelf cavity circulation. The time-evolving sensitivities to changes in the oceanic state reveal dominant time scales over which the shelf exit is connected to the deep interior of the cavity and its ice-ocean interface. The dominant

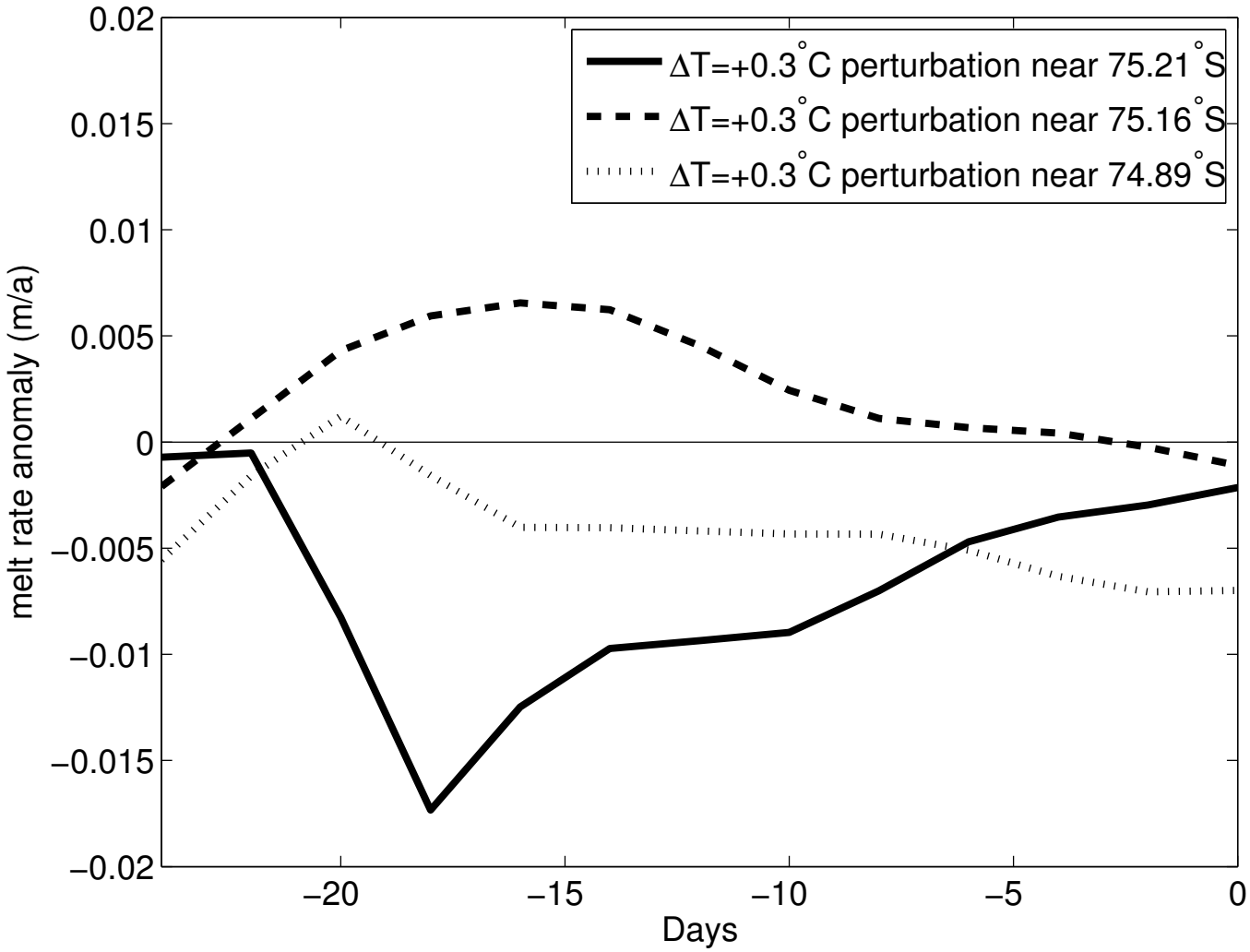

Fig. 6. Time series of melt rate anomalies inferred from three independent finite difference perturbation experiments at the locations considered in Fig. 5. In each case a perturbation of $+0.3^\circ$ was applied in a 4×4×4 grid point box centered around 620 m depth and run forward in time for 26 days.

pathways were found to be highly non-uniform. Topographic effects as a result of rotation are important in connecting outer water mass properties to sub-shelf circulation and to its impact on melt rate changes.

The sensitivity amplitudes are determined by the linearized three-equation melt rate parameterization and may offer insights into the complex interplay between the temperature, salinity, and pressure variations considered here. An important question that one can begin to address is what are the dominant controls on sub-ice shelf melt rates. In doing so, one needs to extend the control space to include those controls whose variations are expected to exert significant changes on our objective function. In the present context of the small PIIS box, a dominant control is clearly the provision of uncertain western hydrographic boundary conditions. The spatial sensitivity pattern which seems to be determined in part by the bathymetry suggest bottom topography as a further control parameter [Losch and Wunsch 2003, Losch and Heimbach 2007], in particular in the light of the recent discovery of a ridge underneath PIIS [Jenkins and others 2010a]. Another source of uncertainty comes from the poorly determined turbulent exchange coefficients for heat and salinity. In the absence of observational constraints they were chosen constant here, but are obvious choices to be added to the space of control variables. We sketched in the Appendix how the adjoint code would change as a result, and hinted that AD would handle this in a straightforward manner. Melt rate itself is an alternative parameter to be estimated directly in an inversion.

The high degree of spatial variability, with regions exhibiting large (and recurring) sensitivities in the vicinity of others with little apparent sensitivities have important implications for observation and monitoring. To the extent that these spatial patterns are robust they provide valuable information for guiding observational campaigns, e.g. for under-ice shelf instrument deployment (e.g., AUV), or the determination of suitable drilling positions on the ice shelf for hydrographic instrument lowering. We advocate that studies such as this should be extended and considered in the mix of decision-making tools for observing system design.

The above discussion implies ways in which the present study can be extended. Putting the PIIS in the context of the regional circulation of the Amundsen Sea and that of the wider Southern Ocean calls for an increase in the domain size to capture in more detail remote oceanic and atmospheric forcings of the PIIS circulation variability. This would also include atmospheric forcings as control variables. Suitable boundary conditions that capture the strong eddy variability of the Antarctic Circumpolar

Current (ACC) could come from optimized regional products such as the Southern Ocean State Estimate [Mazloff and others 2010] or regional very high-resolution ECCO2 products [Schodlok and others 2011]. With these extensions comprehensive estimates of the regional circulation, melt rates and other uncertain parameters from all available hydrographic observations seems possible.

A long-term perspective is the ability to constrain the coupled ocean-ice shelf system in which ocean circulation interacts with ice dynamics, through the combined use of hydrographic and ice shelf observations. Such a coupled estimation system would weigh melt rate changes and thus sub-ice shelf geometry changes mandated by oceanic observations against ice shelf geometry changes imposed by ice flow speed observations, through adjoint sensitivity propagation between the components of the coupled model.

5. ACKNOWLEDGEMENTS

The authors benefited greatly from discussions with and encouragement from Adrian Jenkins, Paul Holland, and Keith Nicholls. We thank Mike Schröder (AWI) for providing the hydrographic data for setting up the model domain. This work is supported in part by the National Science Foundation and the National Aeronautics and Space Administration's continued support of the Estimating the Circulation and Climate of the Ocean (ECCO) projects (ECCO-GODAE and ECCO2).

APPENDIX A. MELT RATE PARAMETERIZATION GRADIENTS

Generating the adjoint code of the melt rate parameterization is the technical innovation of this study. Rather than reproducing the full adjoint model we highlight a few aspects that are related to algorithmic differentiation (AD).

Melt rates under the ice shelf are parameterized via a three-equation system [Hellmer and Olbers 1989, Jenkins and others 2001] for the freshwater flux, the heat flux balance, and the water temperature at the ice-ocean interface:

$$\begin{aligned} -q &= \rho\gamma_S \frac{S - S_b}{S_b} \\ -L\,q &= c_p\rho\gamma_T(T - T_b) \;+\; \rho_I c_p^I \kappa \frac{T_s - T_b}{h} \\ T_b &= (\,0.0901 \;-\; 0.0575\,S_b)^\circ\mathrm{C} \;-\; 7.61\cdot 10^{-4}\,\frac{^\circ\mathrm{C}}{\mathrm{dBar}}\,p \end{aligned} \tag{A1}$$

Here, fresh water flux q is positive upwards, such that negative values indicate ocean freshening.

The melt rate $-q(t)$ is (through S_b) an implicit function of T, S, and p, because the solution of eqn. (A1) involves a quadratic problem for S_b as a function of T, S, p, whose roots have the general structure:

$$S_b \;=\; -B \begin{cases} +A\sqrt{D}, & \text{for } B < A\sqrt{D} \\ -A\sqrt{D}, & \text{for } B > A\sqrt{D} \end{cases} \tag{A2}$$

The coefficient B and discriminant D are functions of T, S, p, whereas A is a function only of the transfer coefficients γ_T, γ_S, which are here assumed constant.

In the following we show that while q is an explicit function of S and S_b, its implicit dependence on T, S, and p is obtained through application of the chain rule, which is at the heart of AD. The total derivative of $q(S(t),\,T(t),\,p(t))$ at a given time t is

$$\begin{aligned} \delta q &= \frac{\rho\gamma_s}{S_b}\,\delta S \;-\; \frac{\rho\gamma_s}{S_b^2}\,\delta S_b \\ &= \frac{\rho\gamma_s}{S_b^2}\,\left\{\left(S_b - \frac{\partial S_b}{\partial S}\right)\delta S \;-\; \frac{\partial S_b}{\partial T}\delta T \;-\; \frac{\partial S_b}{\partial p}\delta p\right\} \end{aligned} \tag{A3}$$

This derivative explicitly depends on S_b itself. Assuming $S_b = \mathrm{O}(30)$ and $\frac{\partial S_b}{\partial S} = \mathrm{O}(1)$, $1 - \frac{1}{S_b}\frac{\partial S_b}{\partial S} > 1$, which explains the opposite signs of $\delta^* T$ and $\delta^* S$ discussed in section 3.2. It is also obvious from eqns. (A2) and (A3) that the derivative code can become arbitrarily complicated.

S_b and thus δq depend on the state itself through coefficients A, B, and D and the relative magnitudes of A, B, and D. Therefore, the control flow requires the evaluation of two derivative expressions subject to a conditional statement (IF-statement). Algorithmic differentiation (AD) ensures correct adjoint code by rigorous application of the chain rule and generation of code for each conditional branch.

So far we have chosen the simplest control space possible that consists only of the model state variables. Various alternatives or extensions are possible. For example, we could add the (unknown) transfer coefficients γ_T and γ_S to the set of control variables. We see immediately, that in this case the derivative expression, eqn. (A3) would need to be augmented as follows:

$$\begin{aligned} \delta q = \; & \frac{\rho\gamma_s}{S_b}\,\delta S \;+\; \frac{\rho S}{S_b}\,\delta\gamma_S \\ & -\; \frac{\rho\gamma_s}{S_b^2}\left\{\frac{\partial S_b}{\partial T}\delta T + \frac{\partial S_b}{\partial S}\delta S + \frac{\partial S_b}{\partial p}\delta p \right. \\ & \qquad \left. + \frac{\partial S_b}{\partial \gamma_T}\delta\gamma_T + \frac{\partial S_b}{\partial \gamma_S}\delta\gamma_S\right\} \end{aligned} \tag{A4}$$

advection scheme	3rd order direct space-time
vertical advection & diffusion	implicit (T, S)
equation of state	Jackett and McDougall [1995]
vertical viscosity	10^{-3} m^2/s
Laplacian viscosity	0.05 (grid-scaled)
bi-harmonic viscosity	0.01 (grid-scaled)
vertical diffusion	5×10^{-5} m^2/s
horizontal diffusion	5 m^2/s
linear bottom drag	0
quadratic bottom drag	2.5×10^{-3}
partial cell factor	0.3
reference density ρ	1035 kg m^{-3}
density of ice	917 kg m^{-3}
latent heat of fusion Λ	334000 J kg^{-1}
heat capacity of water c_p	3998 J kg^{-1} K^{-1}
heat capacity of ice c_p^I	2000 J kg^{-1} K^{-1}
heat conduction coefficient κ	1.54×10^{-6} m^2 s^{-1}
surface temperature T_s	$-20\,^\circ$C
transfer coefficients γ_T	10^{-4} m s^{-1}
transfer coefficient γ_S	$5.05 \times 10^{-3}\gamma_T$

Table 1. Some numerical model parameters and properties of the 1/32° configuration.

This simple case illustrates that the tangent linear and adjoint models are not "unique", even for a fixed forward model, but vary in structure depending on the choice of control variables. For estimation purposes, choosing melt rate directly as a control is an attractive choice, and will be discussed elsewhere.

REFERENCES

Adcroft, A., C. Hill and J. Marshall, 1997. The Representation of Topography by Shaved Cells in a Height Coordinate Model, *Mon. Wea. Rev.*, **125**(9), 2293–2315.

Giering, R. and T. Kaminski, 1998. Recipes for adjoint code construction, *ACM Transactions on Mathematical Software*, **24**, 437–474.

Giering, R., T. Kaminski and T. Slawig, 2005. Generating Efficient Derivative Code with TAF: Adjoint and Tangent Linear Euler Flow Around an Airfoil, *Future Generation Computer Systems*, **21(8)**, 1345–1355.

Griewank, A. and A. Walther, 2008. Evaluating Derivatives. Principles and Techniques of Algorithmic Differentiation, vol. 19 of *Frontiers in Applied Mathematics*, SIAM, Philadelphia, 2nd ed.

Heimbach, P., 2008. The MITgcm/ECCO adjoint modelling infrastructure, *CLIVAR Exchanges*, **44 (Volume 13, No. 1)**, 13–17.

Heimbach, P. and V. Bugnion, 2009. Greenland ice sheet volume sensitivity to basal, surface, and initial conditions, derived from an adjoint model, *Annals Glaciol.*, **50**(52), 67–80.

Heimbach, P., C. Hill and R. Giering, 2005. An efficient exact adjoint of the parallel MIT general circulation model, generated via automatic differentiation, *Future Generation Computer Systems*, **21(8)**, 1356–1371.

Hellmer, H.H., S.S. Jacobs and A. Jenkins, 1998. Oceanic erosion of a floating Antarctic glacier in the Amundson Sea, *Antarctic Res. Ser.*, **75**, 83–99.

Hellmer, H.H and D.J. Olbers, 1989. A two-dimensional model of the thermohaline circulation under an ice shelf, *Antarct. Sci.*, **1**, 325–336.

Holland, D.M. and A. Jenkins, 1999. Modeling thermodynamic ice-ocean interactions at the base of an ice shelf, *J. Phys. Oceanogr.*, **29**(8), 1787–1800.

Holland, P.R., A. Jenkins and D.M. Holland, 2008. The response of ice shelf basal melting to variations in ocean temperature, *J. Clim.*, **21**, 2558–2572.

Jackett, David R. and Trevor J. McDougall, 1995. Minimal Adjustment of Hydrographic Profiles to Achieve Static Stability, *J. Atmos. Ocean. Technol.*, **12**(4), 381–389.

Jenkins, A. and A. Bombosch, 1995. Modeling the effects of frazil ice crystals on the dynamics and thermodynamics of ice shelf water plumes, *J. Geophys. Res.*, **100**(C4), 6967–6981.

Jenkins, A., P. Dutrieux, S.S. Jacobs, S.D. McPhail, J.R. Perrett, A.T. Webb and D. White, 2010a. Observations beneath Pine Island Glacier in West Antarctica and implications for its retreat, *Nature Geosci.*, **3**, 468–472.

Jenkins, A., H.H. Hellmer and D.M. Holland, 2001. The role of melt-water advection in the formulation of conservative boundary conditions at an ice-ocean interface, *J. Phys. Oceanogr.*, **31**, 285–296.

Joughin, I., E. Rignot, C.E. Rosanova, B.K. Lucchitta and J. Bohlander, 2003. Timing of recent accelerations of Pine Island Glacier, Antarctica, *Geophys. Res. Lett.*, **30**, 1760.

Le Dimet, F.-X. and O. Talagrand, 1986. Variational algorithms for analysis and assimilation of meteorological observations: theoretical aspects, *Tellus*, **38A**, 97–110.

Losch, M., 2008. Modeling ice shelf cavities in a z coordinate ocean general circulation model, *J. Geophys. Res.*, **113**, C08043.

Losch, M. and P. Heimbach, 2007. Adjoint sensitivity of an ocean general circulation model to bottom topography, *J. Phys. Oceanogr.*, **37(2)**, 377–393.

Losch, M. and C. Wunsch, 2003. Bottom topography as a control variable in an ocean model, *J. Atmos. Ocean. Technol.*, **20**, 1685–1696.

MacAyeal, D.R., 1992. The basal stress distribution of Ice Stream E, Antarctica, inferred from control methods, *J. Geophys. Res.*, **97(B1)**, 595–603.

MacAyeal, D.R., 1993. A tutorial on the use of control methods in ice-sheet modeling, *J. Glaciol.*, **39(131)**, 91–98.

Marotzke, J., R. Giering, K.Q. Zhang, D. Stammer, C. Hill and T. Lee, 1999. Construction of the adjoint MIT ocean general circulation model and application to Atlantic heat transport variability, *J. Geophys. Res.*, **104, C12**, 29,529–29,547.

Marotzke, J. and C. Wunsch, 1993. Finding the steady state of a general circulation model through data assimilation: Application to the North Atlantic Ocean, *J. Geophys. Res.*, **98, C11**, 20,149–20,167.

Marshall, J., A. Adcroft, C. Hill, L. Perelman and C. Heisey, 1997b. A finite-volume, incompressible Navier Stokes model for studies of the ocean on parallel computers, *J. Geophys. Res.*, **102, C3**, 5,753–5,766.

Marshall, J., C. Hill, L. Perelman and A. Adcroft, 1997a. Hydrostatic, quasi-hydrostatic and nonhydrostatic ocean modeling, *J. Geophys. Res.*, **102, C3**, 5,733–5,752.

Mazloff, M.R., P. Heimbach and C. Wunsch, 2010. An Eddy-Permitting Southern Ocean State Estimate, *J. Phys. Oceanogr.*, **40(5)**, 880–899.

McPhee, M.G., G.A. Maykut and J.H. Morison, 1987. Dynamics and thermodynamics of the ice/upper ocean system in the marginal ice zone of the Greenland Sea, *J. Geophys. Res.*, **92**, 7017–7031.

MITgcm Group, 2011. MITgcm User Manual, *Online documentation*, MIT/EAPS, Cambridge, MA 02139, USA, `http://mitgcm.org/public/r2_manual/latest/online_documents/manual.html`.

Payne, A.J., P.R. Holland, A. Shepherd, I.C. Rutt, A. Jenkins and I. Joughin, 2007. Numerical modeling of ocean-ice interactions under Pine Island Bay's ice shelf, *J. Geophys. Res.*, **112**(C10), C10019.

Payne, A.J., A. Vieli, A.P. Shepherd, D.J. Wingham and E. Rignot, 2004. Recent dramatic thinning of largest West Antarctic ice stream triggered by oceans, *Geophys. Res. Lett.*, **31**, L23401.

Pritchard, H.D., R.J. Arthen, D.G. Vaughan and L.A. Edwards, 2009. Extensive dynamic thinning on the margins of the Greenland and Antarctic ice sheets, *Nature*, **461**, 971–975.

Rignot, E., 1998. Fast recession of a West Antarctic glacier, *Science*, **281**, 549–551.

Rignot, E., 2006. Changes in ice dynamics and mass balance of the Antarctic ice sheet, *Phil. Trans. Roy. Soc. A*, **364**.

Rignot, E., J.L. Bamber, M.R. van den Broeke, C. Davis, Y. Li, W.J. van de Berg and E. van Meijgaard, 2008. Recent Antarctic ice mass loss from radar interferometry and regional climate modelling, *Nature Geosci.*, **1**(106-110).

Robin, G. de Q., 1979. Formation, flow, and disintegration of ice shelves, *J. Glaciol.*, **24**(90), 259–271.

Schodlok, M.P., D. Menemenlis, E.J. Rignot and M. Studinger, 2011. Sensitivity of the ice shelf ocean system to the Pine Island cavity shape measured by IceBridge, *Ann. Glaciol.*, **submitted**, .

Shepherd, A., D.J. Wingham, J.A.D. Mansley and H.F.J. Corr, 2001. Inland thinning of Pine Island Glacier, West Antarctica, *Science*, **291**, 862–864.

Shepherd, A., D. Wingham and E. Rignot, 2004. Warm ocean is eroding West Antarctic ice sheet, *Geophys. Res. Lett.*, **31**, L23402.

Stammer, D., C. Wunsch, I. Fukumori and J. Marshall, 2002b. State estimation in modern oceanographic research, *EOS Transactions AGU*, **83(27)**, 294–295.

Stammer, D., C. Wunsch, R. Giering, C. Eckert, P. Heimbach, J. Marotzke, A. Adcroft, C.N. Hill and J. Marshall, 2002a. The global ocean circulation and transports during 1992 – 1997, estimated from ocean observations and a general circulation model., *J. Geophys. Res.*, **107(C9)**, 3118.

Talagrand, O. and P. Courtier, 1987. Variational assimilation of meteorological observations with the adjoint vorticity equation. I: Theory, *Q. J. R. Meteorol. Soc.*, **113**, 1311–1328.

Thomas, R., E. Rignot, G. Casassa, P. Kanagaratnam, C. Acuna, T. Akins, H. Brecher, E. Frederick, P. Gogineni, W. Krabill, S. Manizade, H. Ramamoorthy, A. Rivera, R. Russell, J. Sonntag, R. Swift, J. Yungel, and J. Zwally, 2004. Accelerated Sea-Level Rise from West Antarctica, *Science*, **306**, 255–258.

Timmermann, R., A. Le Brocq, T. Deen, E. Domack, P. Dutrieux, B. Galton-Fenzi, H. Hellmer, A. Humbert, D. Jansen, A. Jenkins, A. Lambrecht, K. Makinson, F. Niederjasper, F. Nitsche, O. A. Nøst, L. H. Smedsrud and W. H. F. Smith, 2010. A Consistent Data Set of Antarctic Ice Sheet Topography, Cavity Geometry, and Global Bathymetry, *Earth System Science Data*, **2**(2), 261–273.

Tziperman, E. and W.C. Thacker, 1989. An optimal control / adjoint equation approach to studying the ocean general circulation, *J. Phys. Oceanogr.*, **19**, 1471–1485.

Velicogna, I. and J. Wahr, 2006. Measurements of Time-Variable Gravity Show Mass Loss in Antarctica, *Science*, **311**, 1754–1756.

Vieli, A. and J.A. Payne, 2003. Application of control methods for modelling the flow of Pine Island Glacier, West Antarctica, *Ann. Glaciol.*, **36**, 231–237.

Wingham, D.J., A.J. Ridout, R. Scharroo, R.J. Arthern and C.K. Shum, 1998. Antarctic elevation change from 1992 to 1996, *Science*, **282**, 456–458.

Wingham, D.J., D.W. Wallis and A. Shepherd, 2009. Spatial and temporal evolution of Pine Island Glacier thinning, 1995–2006, *Geophys. Res. Lett.*, **36**, L17501.

Wunsch, C., 2006a. Discrete Inverse and State Estimation Problems : With Geophysical Fluid Applications, Cambridge University Press, Cambridge (UK).

Wunsch, C. and P. Heimbach, 2007. Practical global oceanic state estimation, *Physica D*, **230(1-2)**, 197–208.

Wunsch, C., P. Heimbach, R.M. Ponte and I. Fukumori, 2009. The Global General Circulation of the Oceans Estimated by the ECCO-Consortium, *Oceanography*, **22**(2), 88–103.